Aeroacoustic Characterization of Optimum Hovering Rotors using Artificial Neural Networks

Christopher S. Thurman
Research Aerospace Engineer
NASA Langley Research Center
Hampton, VA, USA

Nikolas S. Zawodny
Research Aerospace Engineer
NASA Langley Research Center
Hampton, VA, USA

ABSTRACT

This work illustrates the use of artificial neural network modeling in the aerodynamic and aeroacoustic characterization of optimum hovering rotors over a broad range of design and operating conditions. Design of Experiments was used to create input feature spaces over eight input factors: the number of rotor blades, rotor radius, rotor rotation rate, design thrust condition, collective pitch, airfoil camber, the location of maximum camber, and the airfoil thickness. A low-fidelity tool chain was then used at the discrete data points defined by the designed input feature spaces to analytically design optimum hovering rotors and simulate aerodynamic and aeroacoustic quantities. This allowed for the generation of data sets over which to train and test the artificial neural network prediction models. Prediction models were trained over the data sets for the actual thrust generated by the rotor, power loading, tonal thickness and loading noise at the fundamental blade passage frequency, and broadband self-noise at seventeen one-third octave bands between 1 kHz and 40 kHz. These prediction models were validated by testing over data previously unseen by the models to quantify their capability for generalization to new data within the design feature space. The models were then used to study the effect each input feature had on the aeroacoustics and aerodynamics of optimum hovering rotors, and physical insights were gained to further explain the effect of each input. This characterization study showed that tonal noise and power loading were most sensitive to the number of rotor blades and the rotor rotation rate and that broadband noise was most sensitive to collective pitch and the design thrust condition.

NOTATION

$c(r)$	Rotor chord length distribution, inches
C_T	Thrust coefficient, $\frac{T}{\rho A(\Omega R)^2}$
M	Airfoil maximum camber, percentage of chord
N	Airfoil location of maximum camber, percentage of chord
N_b	Number of rotor blades
$OASPL$	Overall sound pressure level, dB
PL	Power Loading, lb/HP
P_T	Total (i.e., induced and profile) power, HP
R	Rotor tip radius, inches
r	Normalized span location, $\frac{x}{R}$
SPL	Sound pressure level, dB
T_{design}	Design thrust condition, lb
T_{pred}	Predicted rotor thrust, lb
XX	Airfoil thickness, percentage of chord
$\alpha(r)$	Angle of attack distribution, deg
α_0	Airfoil zero lift angle of attack, rad
Ω	Rotor rotational rate, revolutions per minute (RPM)
$\phi_(r)$	Inflow angle distribution, deg
$\sigma(r)$	Rotor solidity distribution, $\frac{N_b c(r)}{\pi R}$
Θ_{obs}	Observer angle relative to rotor plane, deg
$\theta_{tw}(r)$	Rotor twist distribution, deg
θ_0	Collective pitch, deg.

Presented at the Vertical Flight Society's 77th Annual Forum & Technology Display, Virtual Event, May 11–13, 2021.

INTRODUCTION

Demand for small unmanned aerial systems (sUAS) has increased due to their potential for missions such as package delivery and aerial surveillance. When comparing sUAS to traditional helicopters, the relative importance of noise generating mechanisms differs. For example, it has been shown that the stochastic (i.e., broadband) portion of the noise emanating from sUAS vehicles lies in the most perceptible range of human audibility and is a dominant noise source when compared to the deterministic (i.e., tonal) noise, which dominates for traditional helicopters (Refs. 1 and 2).

Many tools exist for predicting both tonal and broadband noise (Refs. 1–4). For modeling tonal noise, a wide range of multifidelity tools exist: panel methods, blade element momentum theory (BEMT), comprehensive analysis codes, traditional Navier-Stokes solvers, and scale-resolving flow simulations. Each of these tools is used to predict unsteady aerodynamic forces. The resulting acoustic pressures are propagated to arbitrary observer locations using an implementation of the Ffowcs Williams and Hawkings (FW-H) equation. Similar approaches have been used to predict broadband noise

directly from unsteady aerodynamic forces using the scale-resolving Lattice-Boltzmann method, though at great computational cost (Refs. 2 and 3). Lower-fidelity methodologies for predicting broadband noise have also been established, such as the theoretical trailing-edge noise model devised by Amiet (Ref. 5) and the semiempirical self-noise prediction methodology devised by Brooks et al. (Ref. 6). However, these low-fidelity broadband noise tools lack the ability to capture more complex aerodynamically induced noise generation associated with rotorcraft (e.g., atmospheric turbulence ingestion noise and blade wake interaction noise). This is due to these models having been developed based upon a wind tunnel campaign of various, fixed, 2-D and 3-D NACA 0012 airfoil sections. Still, self-noise is a dominant broadband noise source, and its study can be beneficial in preliminary analysis and design efforts.

The purpose of the present research was to develop aerodynamic and aeroacoustic prediction models using machine-learning-based approaches to characterize representative sUAS rotors in hover. Specifically, this work focused on rigid optimum hovering rotors. A four-step approach shown in Fig. 1 was adopted in this work.

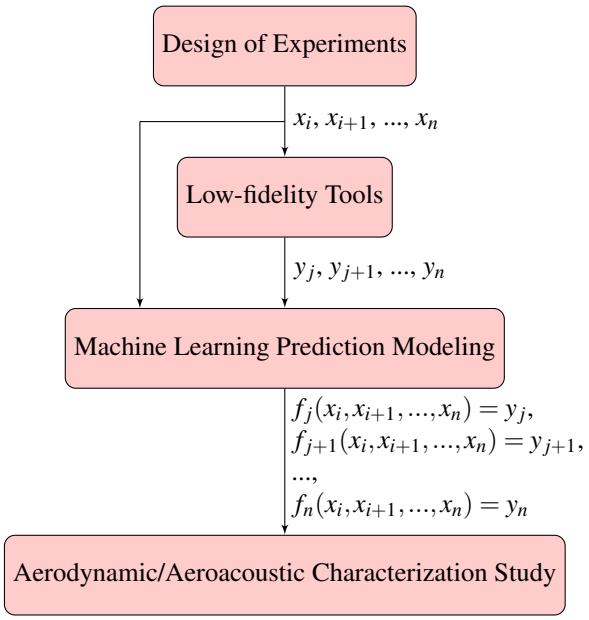

Figure 1: Block diagram representation of technical approach where x_i is the ith input feature, y_j is the jth result using the low-fidelity tools, and f_j is the jth machine learning prediction model.

The first step entailed the use of modern Design of Experiments (DoE) to create an input feature space or design space consisting of discrete combinations of input variable values. The input feature space consisted of various airfoil and rotor geometric parameters as well as flight conditions, which were thought to encapsulate much of the sUAS region of operability. Preexisting low-fidelity tools were then used to predict various aerodynamic and aeroacoustic quantities at the design points prescribed by the feature space. Once these data were generated, machine learning was used to develop prediction models to accurately and quickly predict various aerodynamic and aeroacoustic quantities of particular interest to rotorcraft. Lastly, and most importantly, these prediction models were used in a characterization effort to study the effects of each input feature on both the aerodynamics and aeroacoustic tonal and broadband noise.

TECHNICAL APPROACH

Design of Experiments

DoE is a process used for planning an experiment so that appropriate data can be collected and analyzed by statistical methods, resulting in valid and objective conclusions (Ref. 7). DoE is typically used in systems comprised of multiple inputs when a nonlinear functional relationship between the quantities of interest, such as force and moment coefficients, and the regressors, or inputs, and their interactions is required. DoE can be broken up into two categories: classical and modern. A comprehensive study of both categories of DoE was performed by the author in Ref. 8, which showed the superiority of modern DoE in the context of computer-based experiments, such as those performed in this work.

Modern DoE was used in this work to design a feature space consisting of the following inputs for the aerodynamic prediction models: N_b, R, Ω, T_{design}, θ_0, M, N, and XX. The same input features were used for the aeroacoustic models; however, with the inclusion of the angle between the acoustic observer location and the center of the rotor, Θ_{obs}. There were seven discrete observer locations prescribed along an arc located 1.896 m away from the center of the rotor, similar to the observer array used in Ref. 3. The range and type of each input feature are shown in Table 1.

Table 1: Input feature space. (* indicates categorical factors. All other factors are continuous.)

Input Feature	Range
N_b*	2, 3, 4
R	6 in - 8 in
Ω	3500 RPM - 6000 RPM
T_{design}	1.5 lb - 3.0 lb
θ_0	-5° - $+5^\circ$
M	0% - 9%
N	20% - 50%
XX	6% - 15%
Θ_{obs}*	-45°, -30°, -10°, 0°, $+10^\circ$, $+30^\circ$, $+45^\circ$

Since machine learning prediction modeling is an interpolation problem, it is imperative to spread the input feature design points uniformly throughout the feature space by using various alphabetically optimal designs or space-filling designs. Alphabetic optimality refers to placing design points so that some optimality criterion, such as prediction variance or regressor screening capability, is satisfied. Space-filling designs, such as the Uniform Design (UD), Latin Hyper-Cube

Design, Sphere-Packing Design, etc., spread the design points evenly throughout the region of experimentation, adhering to some measure of uniformity determined by the design being used (Ref. 9). The purpose of this uniform sampling is to acquire data in a manner that represents the entire experimental domain while minimizing the difference of the overall mean between the prediction model and the experimental data (Ref. 10).

A space-filling UD was selected for this work, which minimized the centered L_2 discrepancy between the design points and a theoretical distribution (Ref. 11). Since N_b is a discrete (i.e., categorical) factor, three designs were created, one at each discrete value of N_b, for a total of 144 design points. The ensemble of these designs was used as the training set for the machine learning prediction models. It is common in machine learning to split the data set into training and testing data; however, when using DoE, this data split may produce bias toward specific regions of the design space. For example, if all split training data are located in a particular quadrant of the design space, there will be inadequate coverage over the entirety of the design space to train the prediction model. For this reason, a separate design space was created over the same input feature space for the test data, which contained 48 points. The low-fidelity tools discussed in the subsequent section were then used to simulate the prescribed design points, and machine learning was used to create aerodynamic and aeroacoustic prediction models with functional relationships to the defined input features.

Low-Fidelity Tools

Throughout this work, various low-fidelity tools were utilized to allow for rotor designs comprised of the NACA four-digit airfoil geometric parameters: the camber, M, location of maximum camber, N, and thickness, XX, as well as characteristic rotor properties such as the rotor radius, R, number of blades, N_b, design thrust condition, T_{design}, collective pitch, θ_0, and rotor rotation rate, Ω. The aerodynamic prediction tool, XFOIL, was used to calculate a zero lift angle of attack, α_0, based upon the airfoil properties. These properties were used in conjunction with the rotor properties and Eq. 1 from Ref. 12 to calculate the rotor blade twist distribution of an optimum hovering rotor with a tip chord length, c_{tip}, of 0.5 in:

$$\theta_{tw}(r) = \frac{1}{r}\left(\frac{4C_{T_{design}}}{5.73\sigma(r)} + \sqrt{\frac{C_{T_{design}}}{2}}\right) - \alpha_0, \qquad (1)$$

where r is the normalized span location and $C_{T_{design}}$ is the thrust coefficient calculated using T_{design}.

An optimum hovering rotor can be defined as one that has both minimal induced power requirements and minimal profile power requirements. Equation 1 is such that the rotor induces uniform inflow, satisfying the induced power requirement. To satisfy the profile power requirement, the chord distribution of the rotor, $c(r)$, follows that of Eq. 2 from Ref. 12, which allows for each radial station to operate at an optimal lift to drag ratio:

$$c(r) = \frac{c_{tip}}{r}, \qquad (2)$$

where r is the normalized span location.

Since this optimum chord distribution is generally not physically realizable, a linear taper ratio of 2.5 to 1 was selected for this work. This linear taper ratio was thought to best replicate the taper of an optimum hovering rotor over the outboard 25% span of the rotor, as shown in Fig. 2. The chord dimension in this plot has not been nondimensionalized since $c(r)$ is constant for all designed rotors.

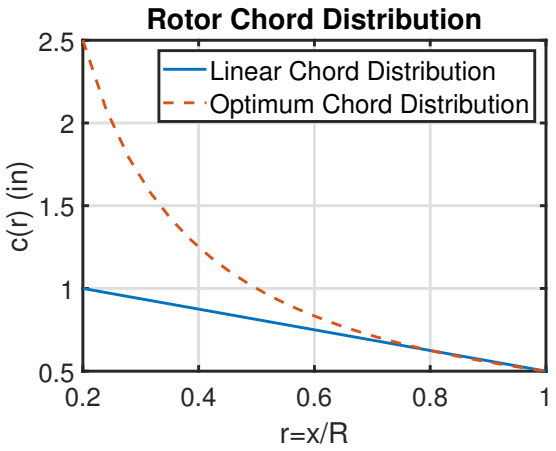

Figure 2: Comparison of 2.5 to 1 linear taper ratio to the taper ratio of an optimum hovering rotor.

ANOPP's Propeller Analysis System (PAS) (Ref. 13) was used to calculate the aerodynamic thrust generated by the rotor, T_{pred}, and the total (i.e., induced and profile) power, P_T, needed by the rotor, tonal (i.e., thickness and loading) noise on a dB basis at the fundamental blade passage frequency (BPF), and finally, various rotor inflow parameters, such as the induced inflow angle distribution, $\phi(r)$, and angle of attack distribution, $\alpha(r)$. These inflow parameters were then used within ANOPP2's Self-Noise Internal Functional Module (ASNIFM) (Ref. 14) to calculate the broadband self-noise, also on a dB basis. ANOPP's PAS and ASNIFM, which is an implementation of the semiempirical prediction methodology devised by Brooks et al. in Ref. 6, were selected based upon their promising prediction accuracy. These low-fidelity tools allowed for the generation of aerodynamic and aeroacoustic data sets, which were vital to the machine learning prediction modeling approach used in this research.

Machine Learning Methodology

Artificial Neural Networks (ANNs) were chosen as the prediction models used to fit the data within the design space; more specifically, Multilayer Perceptrons (MLP) were used. The MLP aims to replicate the architecture of the neurons in the human brain, set up in layers as shown in Fig. 3. Each "hidden" layer consists of a number of activation functions, or neurons, aligned in parallel. All of the neurons of a particular layer are activated in unison, with different multiplicative

weights along the connections between neurons, inputs, and outputs.

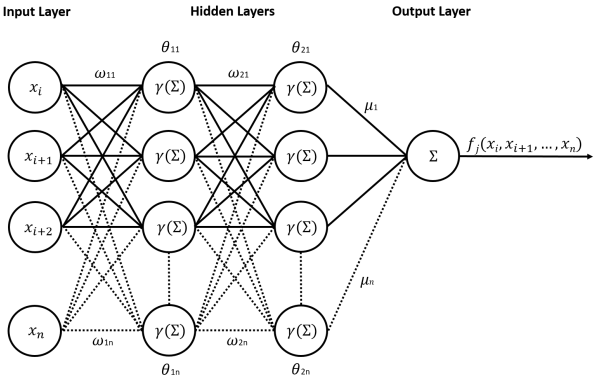

Figure 3: Generic ANN representation where x_i is the ith input feature, ω and μ are multiplicative weights, Σ is a summation operator, γ is the activation function evaluated over the summed inputs multiplied by their respective weights, θ are the hidden layers, and f_j is the jth ANN prediction model.

The machine learning procedures used throughout this work were performed using Google's TensorFlow platform (Ref. 15). The MLP architecture used for all prediction models contained two hidden layers consisting of 100 exponential linear units (ELU) with a linear activation function in the output layer. These ELU were selected over the commonly used rectified linear unit (ReLU) as they are less prone to vanishing gradients and have better overall convergence trends with more accurate results (Ref. 16). The number and type of activation functions used are heuristically determined. It should be noted that ANNs of different architectures and consisting of different activation functions were investigated; however, those mentioned previously were determined to perform optimally for this work.

It was first imperative to rescale each input feature listed in Table 1 to a common basis to eliminate any bias in the optimization procedure of the cost function. To achieve a common basis, each feature was scaled such that it had a mean of zero and a variance of one. The input layer contained values of these scaled inputs at each discrete point in the feature space, which were then passed through the MLP over 1250 epochs, or cycles through the training data. The multiplicative weights along the connections were modified after each epoch until the specified cost function, in our case, the mean absolute error (MAE), was sufficiently minimized using the Adam optimization algorithm (Ref. 17).

Two types of regularization were used on each of the hidden layers: L_2 regularization and a 20% dropout. The L_2 regularization acted to constrain the multiplicative weights. The 20% dropout randomly eliminated 20% of the activation functions in each hidden layer during the training procedure at each epoch (Ref. 18). Regularization is vital to any machine learning procedure in that it aids in reducing the prediction model's bias toward the training data and aids in promoting better generalization to new data. An early stopping criterion was also imposed on the learning procedure to further reduce the possibility of overfitting. A 10-fold cross-validation method was used where the training data were randomly split into ten equally sized partitions. Ten prediction models were then fit over a different set of nine partitions, using the last partition for accuracy evaluation at each epoch during training. These ten models were then evaluated over the test data set, which had not been previously seen by the models, and the model with the highest prediction accuracy was retained.

Because N_b was a categorical factor, one-hot encoding was used, which treated this input feature as three binary inputs. For example, for a two-bladed rotor, the input correspondent to a two-bladed rotor would hold a value of one and the other two inputs correspondent to three- and four-bladed rotors, respectively, would hold values of zero. For the aeroacoustic prediction models, one-hot encoding was also used for Θ_{obs}. Since the data were acquired over all seven observer angles for each design point in the feature space, all design points were replicated for each observer location and their ordering was randomized prior to the training procedure.

Since this work focused on aerodynamic and aeroacoustic characterization, two prediction models were produced for aerodynamics, one for T_{pred}, and one for power loading (PL), or the ratio of T_{pred} to P_T. Only the prediction model for PL was used for aerodynamic characterization throughout this work; however, generating a prediction model for T_{pred} allows for the future calculation of aerodynamic quantities of particular importance to rotorcraft, such as the induced power, profile power, and torque. It should be noted here that T_{design} was used solely for the design of the rotor and T_{pred} includes additional aerodynamic effects caused by the airfoil geometry and θ_0. Two models were created for the tonal noise at the fundamental BPF, one for the thickness noise and one for the loading noise, both on an overall sound pressure level (OASPL) basis. For the broadband noise, separate prediction models were created for each one-third octave band between 1 kHz and 40 kHz, totaling seventeen broadband noise prediction models.

RESULTS

Prediction Model Performance and Validation

An accuracy score produced using Eq. 3 was calculated over the test data and is shown in Table 2. For brevity, these quantities were averaged over the seventeen prediction models for the broadband one-third octaves:

$$Prediction\ Accuracy = 100 * \left(1 - \frac{1}{n}\sum_{i=1}^{n}\left|\frac{y_i - f_i}{y_i}\right|\right), \quad (3)$$

where n is the number of test data values, y_i is the test data value, and f_i is the predicted value.

Table 2 shows that the prediction accuracy values are above 95% for all aeroacoustic models (e.g., $OASPL_{thickness}$, $OASPL_{loading}$, and $SPL_{1/3_{broadband}}$). This signifies that these

models have adequately learned the underlying functional relationships between the inputs and outputs and that they generalize exceptionally well to new data within the feature space. Both aerodynamic models (e.g., PL and T_{pred}) have prediction accuracy values of approximately 85%, which is sufficient for the purposes of this study. Since characterization is the goal of this effort, the aerodynamic models are used to assess general behavioral trends of aerodynamic performance with favorable aeroacoustic behavior; therefore, prediction accuracy scores above 80% are thought to be adequate for this work.

Table 2: Prediction model fit summary.

Prediction Model	Prediction Accuracy
PL	85.89%
T_{pred}	85.62%
$OASPL_{thickness}$	98.16%
$OASPL_{loading}$	97.09%
$SPL_{1/3_{broadband}}$	95.79%

As a further validation, an arbitrary design point within the feature space was selected to compare predicted results to results generated using the low-fidelity tools. The aerodynamic results from the low-fidelity tools were $T_{pred} = 3.43$ lb and $PL = 16.47$ lb/HP and the results predicted using the ANNs were $T_{pred} = 3.22$ lb and $PL = 16.73$ lb/HP. The OASPL of the broadband noise between 1 kHz and 40 kHz was calculated and Fig. 4 shows the comparison between the ANN predicted results and the results generated from the low-fidelity tools for the thickness, loading, and broadband noise at all observer locations. The agreement between the results from the ANN prediction models and the results generated using the low-fidelity tools is consistent with the high prediction accuracy values shown in Table 2.

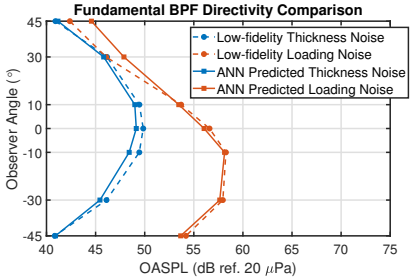

(a) Tonal noise comparison.

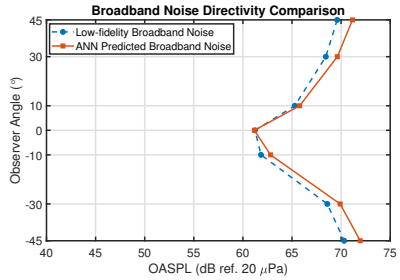

(b) Broadband noise comparison.

Figure 4: Acoustic directivity comparison between ANN predicted results and results from low-fidelity tools. $N_b = 3$, $R = 7$ in, $T_{design} = 2.5$ lb, $\Omega = 5000$ RPM, $M = 6\%$, $N = 40\%$, $XX = 12\%$, and $\theta_0 = 3°$.

Aeroacoustic Rotor Characterization

To compare the effects of each input feature on the rotor acoustics, the ANNs were used to predict acoustic directivities of the tonal thickness, tonal loading, and broadband OASPL at the maximum and minimum values of each input feature defined in Table 1. All other input features were maintained at their mean values. These acoustic directivity plots were generated using the same scaling to allow for a more direct visual comparison. Predictions using the mean values for all input features were also plotted to further illustrate the variation in tonal and broadband noise caused by each input feature. Additionally, Eq. 1 and ANOPP's PAS were used to develop plots for the twist distribution, $\theta_{tw}(r)$, inflow angle distribution, $\phi(r)$, and angle of attack distribution, $\alpha(r)$, at the maximum, minimum, and mean values of each input feature. This was done to provide physical insight as to why the input features affect the rotor acoustics. Separate plots have been created for each input feature in Figs. 5–9, which show the aerodynamic and aeroacoustic quantities. Examining subfigures (a) and (b) in Figs. 5–9, it can be seen that for an optimum hovering rotor, tonal noise is dominated by the loading noise, implying that input features that produce greater variations to the loading noise are highly influential to the entire tonal noise signature.

It can also be ascertained by comparing Figs. 5–9 that the value of N_b has the greatest effect on tonal loading noise with decreasing values of N_b causing an increase in BPF amplitude. Since $\theta_{tw}(r)$ from Eq. 1 has functional dependence on $C_{T_{design}}$ and σ, decreasing the number of rotor blades while maintaining the same value of T_{design} would decrease the value of σ. Figure 5 shows that decreasing the value of N_b causes an increase in the distributions of $\theta_{tw}(r)$ and $\alpha(r)$, resulting in increased tonal thickness noise, loading noise, and broadband noise. Similarly, Fig. 6 shows that increasing the value of R resulted in a decrease in the value of σ and a decrease in the distributions of $\theta_{tw}(r)$, $\phi(r)$, and $\alpha(r)$. Increasing the value of R would also result in an increased tip Mach number for a fixed value of Ω. The combination of these opposing geometric effects caused by increasing the value of R resulted in a slight increase to tonal noise and a decrease in broadband noise. However, both the tonal loading and broadband noise are less sensitive to R than to N_b. Although $\theta_{tw(r)}$, $\alpha(r)$, and the tonal thickness noise vary similarly with increasing values of R and decreasing values of N_b, the decrease in $\phi(r)$ caused by increasing the value of R was thought to alleviate the effect of the increased tip Mach number on the tonal loading noise, explaining why variations of N_b have a greater effect on tonal loading noise than variations of R. In summary, the value of σ has a dominant effect on the tonal noise with N_b having a greater effect when compared to R, regardless of the similar dependence of σ on both of these input features.

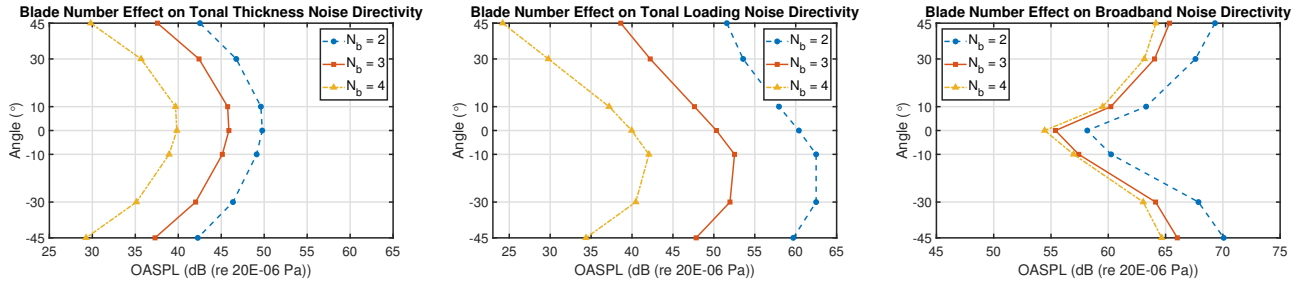

(a) Tonal thickness noise. (b) Tonal loading noise. (c) Broadband noise.

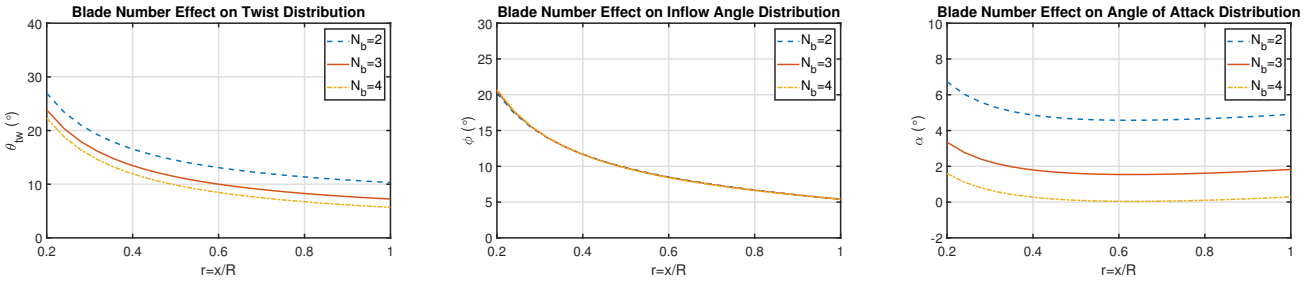

(d) Twist distribution. (e) Inflow angle distribution. (f) Angle of attack distribution.

Figure 5: Blade number effect on tonal noise directivity, broadband noise directivity, twist distribution, inflow angle distribution, and angle of attack distribution. $R = 7$ in, $T_{design} = 2.25$ lb, $\Omega = 4750$ RPM, $M = 4.5\%$, $N = 35\%$, $XX = 10.5\%$, and $\theta_0 = 0°$.

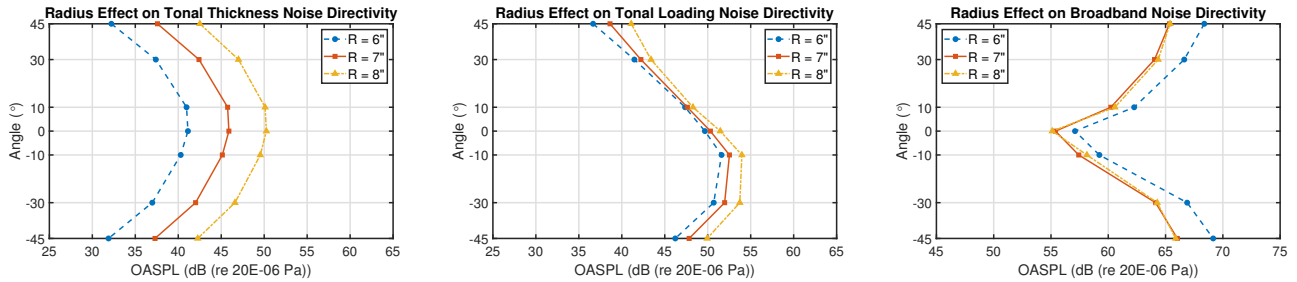

(a) Tonal thickness noise. (b) Tonal loading noise. (c) Broadband noise.

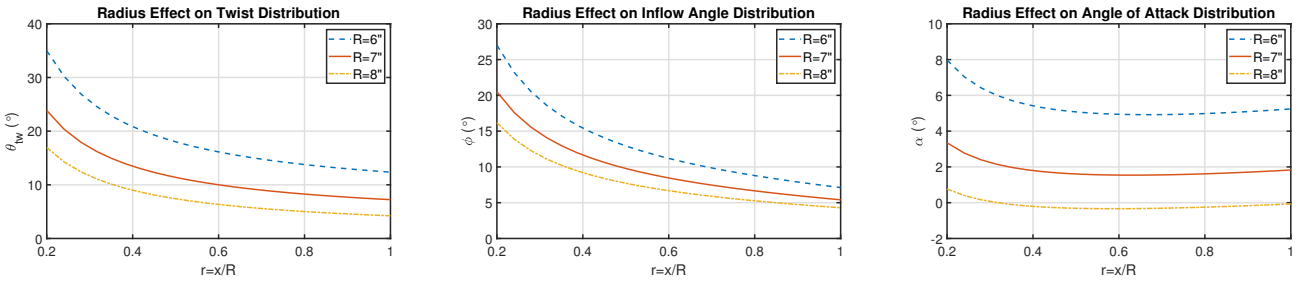

(d) Twist distribution. (e) Inflow angle distribution. (f) Angle of attack distribution.

Figure 6: Radius effect on tonal noise directivity, broadband noise directivity, twist distribution, inflow angle distribution, and angle of attack distribution. $N_b = 3$, $T_{design} = 2.25$ lb, $\Omega = 4750$ RPM, $M = 4.5\%$, $N = 35\%$, $XX = 10.5\%$, and $\theta_0 = 0°$.

Figure 7 shows that the second most significant input feature to the tonal noise is Ω. Although increasing the value of Ω decreases the distributions of $\theta_{tw}(r)$, $\phi(r)$, and $\alpha(r)$ while increasing the tip Mach number, its effect on the tonal thickness noise is much more pronounced than for variations of N_b and R, elucidating the high significance of this input feature on the acoustic results. The effect of varying Ω on the tonal loading noise, shown in Fig. 7b, can also be seen to have a greater significance than for variations of R and lesser significance than for variations of N_b.

Variations of θ_0 affect the tonal loading noise in a similar fashion to variations of Ω with negligible change to the tonal thickness noise for changes in the value of θ_0. Figure 8b shows large variations in the tonal loading noise, thought to be caused by the increasing distributions of $\theta_{tw}(r)$, $\phi(r)$, and $\alpha(r)$. Figure 8c also shows that variations of θ_0 have the

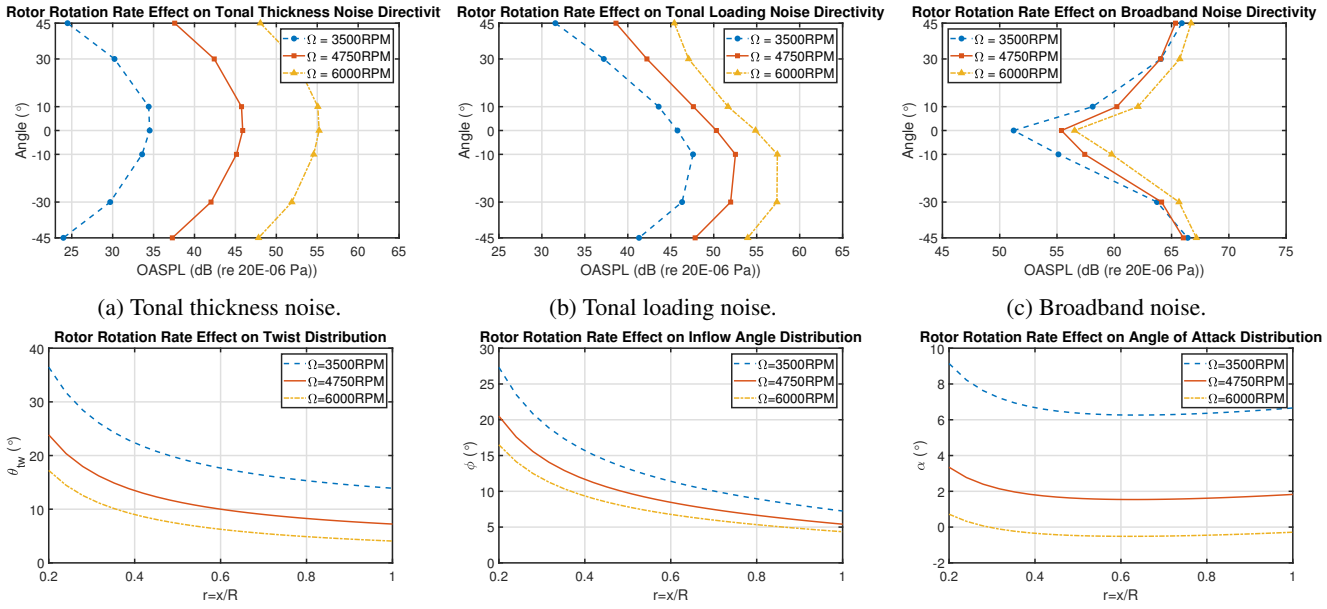

(a) Tonal thickness noise.

(b) Tonal loading noise.

(c) Broadband noise.

(d) Twist distribution.

(e) Inflow angle distribution.

(f) Angle of attack distribution.

Figure 7: Rotor rotation rate effect on tonal noise directivity, broadband noise directivity, twist distribution, inflow angle distribution, and angle of attack distribution. $N_b = 3$, $R = 7$ in, $T_{design} = 2.25$ lb, $M = 4.5\%$, $N = 35\%$, $XX = 10.5\%$, and $\theta_0 = 0°$.

greatest effect on the broadband self-noise. The increased distributions of $\phi(r)$ and $\alpha(r)$ were believed to give rise to the broadband self-noise mechanism, trailing edge separation noise (Ref. 6), which could explain the large sensitivity of broadband noise to variations of θ_0. Increasing the value of T_{design} was seen to have an almost identical trend on the aerodynamics and aeroacoustics as increasing the value of θ_0, so plots for T_{design} were omitted.

Increases in the value of M serve to increase α_0, which would increase the thrust generated by the rotor while reducing the distribution of $\alpha(r)$ for a given thrust value. Figure 9 shows that increasing the value of M decreases the distributions of both $\theta_{tw}(r)$ and $\alpha(r)$, resulting in a slight increase in tonal loading noise and a minimal decrease in broadband noise. Increasing XX was seen to have no impact on the distributions of $\theta_{tw}(r)$ and $\phi(r)$ with very negligible effects on the distribution of $\alpha(r)$. Increasing the value of XX increased the tonal thickness noise but resulted in an almost identical trend in the tonal loading noise and broadband noise as for increasing the value of M, so these plots were excluded. Lastly, variations of N had a negligible effect on all aerodynamic and aeroacoustic quantities so plots for N were also excluded for brevity.

Table 3 shows PL results at the previously defined maximum and minimum values for each input feature. For reference, $PL = 17.55$ lb/HP is the predicted value with all input features retained at their mean values. Larger values of PL indicate superior rotor performance since the rotor would require less power to generate the same amount of thrust. It can be seen that decreasing the value of N_b not only increases the acoustic results, but it also significantly increases the value of PL for a fixed thrust condition. This is due to the decreased power required to rotate fewer blades, which dominates over

Table 3: Power loading at maximum and minimum input feature values.

Input Feature	PL (lb/HP) Min.	PL (lb/HP) Max.
N_b	19.61	16.70
R	18.52	16.61
Ω	20.09	15.23
T_{design}	17.98	17.11
θ_0	18.00	17.08
M	17.73	17.36
N	17.42	17.69
XX	17.16	17.94

aerodynamic effects on the required power caused by increasing the distributions of $\theta_{tw}(r)$ and $\alpha(r)$. Similarly, less power is required for a lower value of R; however, unlike variations of N_b, decreasing the value of R has a favorable effect on the tonal noise with slight adverse broadband noise effects. Table 3 shows that variations of Ω have the greatest effect on PL, with its reduction significantly increasing the rotor efficiency while decreasing the rotor noise. Since variations of both θ_0 and T_{design} had a direct impact on the distributions of $\theta_{tw}(r)$, $\phi(r)$, and $\alpha(r)$, decreasing these input features not only decreases both tonal and broadband noise, but also increases the value of PL, signifying increased rotor performance. Variations of M have a very modest effect on the value of PL, causing a decrease in rotor performance with an increase in the value of M. Variations of N and XX also have a minimal effect on the value of PL with a degradation in rotor performance for decreasing values of N and XX.

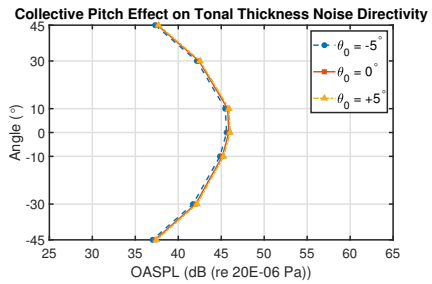

(a) Tonal thickness noise.

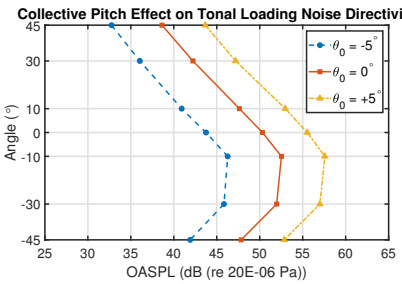

(b) Tonal loading noise.

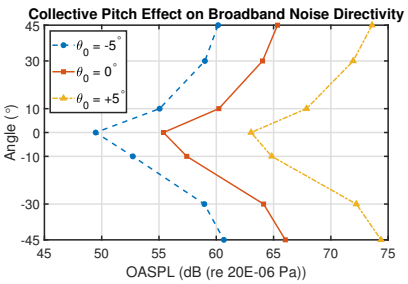

(c) Broadband noise.

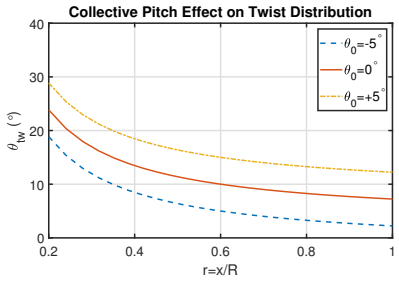

(d) Twist distribution.

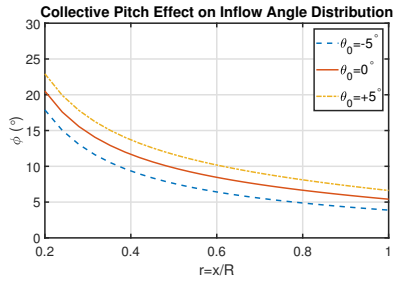

(e) Inflow angle distribution.

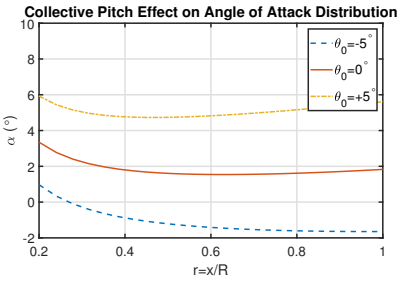

(f) Angle of attack distribution.

Figure 8: Collective pitch effect on tonal noise directivity, broadband noise directivity, twist distribution, inflow angle distribution, and angle of attack distribution. $N_b = 3$, $R = 7$ in, $T_{design} = 2.25$ lb, $\Omega = 4750$ RPM, $M = 4.5\%$, $N = 35\%$, and $XX = 10.5\%$.

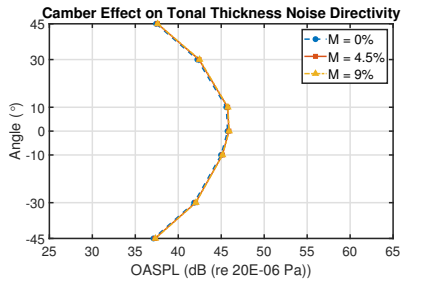

(a) Tonal thickness noise.

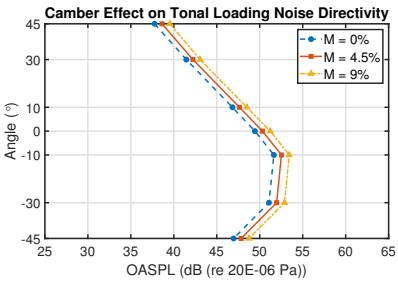

(b) Tonal loading noise.

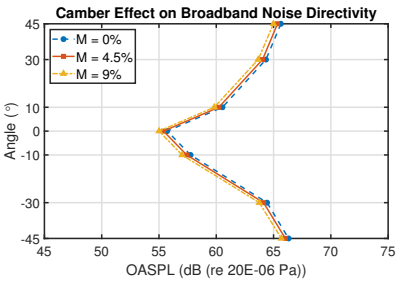

(c) Broadband noise.

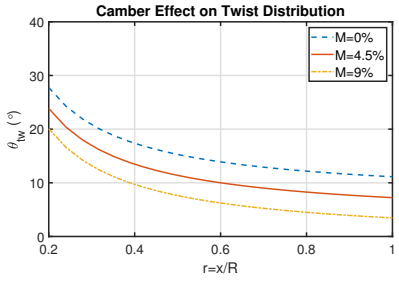

(d) Twist distribution.

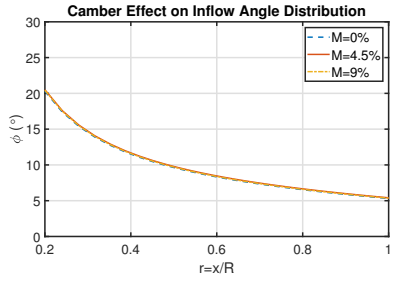

(e) Inflow angle distribution.

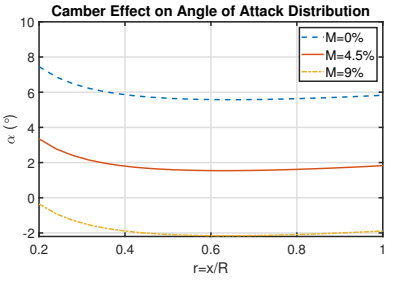

(f) Angle of attack distribution.

Figure 9: Camber effect on tonal noise directivity, broadband noise directivity, twist distribution, inflow angle distribution, and angle of attack distribution. $N_b = 3$, $R = 7$ in, $T_{design} = 2.25$ lb, $\Omega = 4750$ RPM, $N = 35\%$, $XX = 10.5\%$, and $\theta_0 = 0°$.

CONCLUSIONS

This research illustrates the use of machine-learning-based prediction modeling in characterizing the aerodynamics and aeroacoustics of rigid optimum hovering rotors over a broad range of design and operating conditions. A low-fidelity toolchain was established to first allow for the analytical design of optimum hovering rotors based upon the following input features: N_b, R, Ω, T_{design}, θ_0, M, N, and XX. This low-fidelity toolchain consisted of ANOPP's PAS (Ref. 13) to calculate the aerodynamic thrust generated by the rotor, the total (i.e., induced and profile) power needed by the rotor, tonal (i.e., thickness and loading) noise at the fundamental blade passage frequency (BPF), and rotor inflow parameters, such as the distributions of $\phi(r)$ and $\alpha(r)$. The toolchain used the rotor inflow parameters to calculate broadband self-noise using ASNIFM (Ref. 14). Modern DoE was then employed to cre-

ate two uniform, space-filling input feature spaces consisting of discrete data points at different combinations of the defined input features. The low-fidelity tools were used to simulate the data points defined by the two design spaces to develop training and testing data sets for the machine learning prediction models.

Artificial Neural Networks (ANNs) were trained over the data sets to model functional relationships between the input features and aerodynamic/aeroacoustic quantities of interest. The ANNs were used to predict *PL*, tonal thickness and loading OASPL values, and broadband OASPL values along an arc of observers located 1.896 m away from the center of the rotor plane. Equation 1 and ANOPP's PAS were also used to develop distributions of $\theta_{tw}(r)$, $\phi(r)$, and $\alpha(r)$ to establish physical aerodynamic insight. These predictions were conducted at maximum and minimum values of each respective input feature while maintaining all other features at their mean values, which allowed for a visual comparison of the effect of each input feature on the acoustic metrics. Values of *PL* at the maximum and minimum values of each input were also tabulated to gain further insight as to how rotor performance varied with changing input feature values.

It was shown that for an optimal hovering rotor, the tonal noise was dominated by loading noise and that the value of N_b had the greatest effect on the tonal noise. Decreasing the value of N_b decreased the value of σ for a fixed value of T_{design}, which increased the distribution of $\theta_{tw}(r)$ and decreased the distribution of $\alpha(r)$. These effects significantly increased the tonal loading noise while also increasing the value of *PL*, signifying an increase in rotor performance. Increasing the value of R had a similar effect on the acoustics as decreasing the value of N_b since this also decreased the value of σ, but with a degradation in rotor performance. Increasing the value of Ω increased both the tonal and broadband noise while decreasing the distributions of $\theta_{tw}(r)$, $\phi(r)$, $\alpha(r)$, and *PL*, which was attributed to higher tip Mach numbers. Both variations in θ_0 and T_{design} had similar effects on the distributions of $\theta_{tw}(r)$, $\phi(r)$, and $\alpha(r)$, causing an increase in tonal and broadband noise with a degradation in rotor performance. It was shown that the broadband noise was most sensitive to variations of θ_0. The increase in both the distributions of $\phi(r)$ and $\alpha(r)$ was thought to increase broadband trailing edge separation noise, explaining the large sensitivity of broadband noise to variations of θ_0. Increasing the value of M was seen to reduce the distributions of $\theta_{tw}(r)$ and $\alpha(r)$, which caused a minimal increase in tonal noise while slightly decreasing both broadband noise and the value of *PL*. Increasing the value of *XX* had a very similar effect as increasing the airfoil camber, so plots for this input feature were excluded from this work. The plots for N were also omitted since variations in N had negligible effects on all acoustic quantities and *PL*.

It can be concluded from this study that most of the input features modified the twist distribution of an optimum hovering rotor resulting in changes to both the rotor acoustics and performance. The tonal noise and *PL* were most sensitive to N_b and Ω and the broadband noise was most sensitive to θ_0 and T_{design}. Since these ANNs can be used to predict aerodynamic/aeroacoustic quantities of interest in a matter of seconds, it is anticipated that they will be used for future design optimization studies for optimum hovering rotors.

Author contact: Christopher S. Thurman,
Christopher.Thurman@nasa.gov

ACKNOWLEDGMENTS

This work was funded by the NASA Revolutionary Vertical Lift Technology (RVLT) project.

REFERENCES

1. Zawodny, N. S., Boyd Jr., D. D., and Burley, C. L., "Acoustic Characterization and Prediction of Representative, Small-Scale Rotary-Wing Unmanned Aircraft System Components," AHS International 72nd Annual Forum, West Palm Beach, FL, May 2016.

2. Thurman, C. S., Zawodny, N. S., and Baeder, J. D., "Computational Prediction of Broadband Noise from a Representative Small Unmanned Aerial System Rotor," VFS International 76th Annual Forum & Technology Display, Virginia Beach, Virginia, October 2020.

3. Thurman, C. S., Zawodny, N. S., Pettingill, N. A., Lopes, L. V., and Baeder, J. D., "Physics-informed Broadband Noise Source Identification and Prediction of an Ideally Twisted Rotor," 2020 SciTech Forum: AIAA Aeroacoustics Conference, Nashville, Tennessee, January 2021.

4. Li, S., and Lee, S., "UCD-QuietFly: A New Program to Predict Multi-Rotor eVTOL Broadband Noise," 2020 VFS Aeromechanics for Advanced Vertical Flight Technical Meeting, San Jose, California, January 2020.

5. Amiet, R., "Acoustic Radiation from an Airfoil in a Turbulent Stream," *Journal of Sound and Vibration*, Vol. 41, (4), 1975, pp. 407–420.

6. Brooks, T. F., Pope, D. S., and Marcolini, M. A., "Airfoil Self-Noise and Prediction," NASA RP 1218, 1989.

7. Montgomery, D. C., *Design and analysis of experiments*, John Wiley & Sons, 2017.

8. Thurman, C. S., and Somero, J. R., "Comparison of Meta-Modeling Methodologies through the Statistical-Empirical Prediction Modeling of Hydrodynamic Bodies," *Ocean Engineering*, Vol. 210, 2020.

9. Myers, R. H., Montgomery, D. C., and Anderson-Cook, C. M., *Response surface methodology: process and product optimization using designed experiments*, John Wiley & Sons, 2016.

10. Fang, K.-T., Li, R., and Sudjianto, A., *Design and modeling for computer experiments*, Chapman and Hall/CRC, 2005.

11. Hickernell, F., "A generalized discrepancy and quadrature error bound," *Mathematics of Computation of the American Mathematical Society*, Vol. 67, (221), 1998, pp. 299–322.

12. Leishman, J. G., *Principles of Helicopter Aerodynamics*, Cambridge University Press, New York, NY, 2000.

13. Nguyen, L. C., and Kelly, J. J., "A Users Guide for the NASA ANOPP Propeller Analysis System," NASA CR 4768, 1997.

14. Lopes, L., and Burley, C., "ANOPP2 User's Manual: Version 1.2," NASA TM 2016-219342, 2016.

15. Abadi, M., Agarwal, A., Barham, P., Brevdo, E., Chen, Z., Citro, C., Corrado, G. S., Davis, A., Dean, J., Devin, M., Ghemawat, S., Goodfellow, I., Harp, A., Irving, G., Isard, M., Jia, Y., Jozefowicz, R., Kaiser, L., Kudlur, M., Levenberg, J., Mané, D., Monga, R., Moore, S., Murray, D., Olah, C., Schuster, M., Shlens, J., Steiner, B., Sutskever, I., Talwar, K., Tucker, P., Vanhoucke, V., Vasudevan, V., Viégas, F., Vinyals, O., Warden, P., Wattenberg, M., Wicke, M., Yu, Y., and Zheng, X., "TensorFlow: Large-Scale Machine Learning on Heterogeneous Systems," Software available from tensorflow.org, 2015.

16. Clevert, D.-A., Unterthiner, T., and Hochreiter, S., "Fast and Accurate Deep Network Learning by Exponential Linear Units (ELUs)," 4th International Conference on Learning Representations. San Juan, Puerto Rico, May 2016.

17. Kingma, D. P., and Lei Ba, J., "Adam: A Method for Stochastic Optimization," 3rd International Conference on Learning Representations. San Diego, California, May 2015.

18. Srivastava, N., Hinton, G., Krizhevsky, A., Sutskever, I., and Salakhutdinov, R., "Dropout: A Simple Way to Prevent Neural Networks from Overfitting," *Journal of Machine Learning Research*, Vol. 15, (56), 2014, pp. 1929–1958.